CATR Quiet Zone Modelling and the Prediction of "Measured" Radiation Pattern Errors:

Comparison using a Variety of Electromagnetic Simulation Methods

C.G. Parini, R. Dubrovka
Queen Mary University of London
School of Electronic Engineering and Computer Sciences
Peter Landin Building,
London UK E1 4FZ
c.g.parini@qmul.ac.uk, r.dubrovka@qmul.ac.uk

S.F. Gregson
Nearfield Systems Inc.
19730 Magellan Drive,
Torrance, CA 90502-1104 USA
sgregson@nearfield.com

***Abstract*—The successful design and implementation of a compact antenna test range (CATR) is predicated upon the availability of highly accurate and precise computational electromagnetic (CEM) modelling tools. As the accuracy of these models is paramount to both the design of the CATR and the subsequent determination of the facility level uncertainty budget, this paper presents an accuracy evaluation of five different CEM simulations. We report results using methods of CATR modelling including: geometrical-optics with geometrical theory of diffraction, plane-wave spectrum, Kirchhoff-Huygens and current element, before presenting results of their use in the far-field antenna pattern measurement prediction for given CATR-AUT combinations.**

I. Introduction

The single-offset compact antenna test range (CATR) is a widely deployed technique for broadband characterization of electrically large antennas at reduced range lengths [1]. The nature of the curvature and position of the offset parabolic reflector as well as the edge geometry ensures that the resulting collimated field is comprised of a pseudo transverse electric and magnetic (TEM) wave. Thus, by projecting an image of the feed at infinity, the CATR synthesizes the type of wave-front that would be incident on the antenna under test (AUT) if it were located very much further away from the feed than is actually the case with the coupling of the plane-wave into the aperture of the AUT creating the classical measured "far-field" radiation pattern. The accuracy of a pattern measured using a CATR is primarily determined by the phase and amplitude quality of the pseudo plane-wave incident on the AUT aperture, with this being restricted by two main factors: amplitude taper (which is imposed by the pattern of the feed), and reflector edge diffraction, which usually manifests as a high spatial frequency ripple in the pseudo plane wave [2]. It has therefore become customary to specify CATR performance in terms of amplitude taper, and amplitude & phase ripple of this wave over a volume of space, termed the quiet-zone (QZ). Unfortunately, in most cases it is not directly apparent how a given QZ performance specification will manifest itself on the resulting antenna pattern measurement. However, with the advent of powerful digital computers and highly-accurate computational electromagnetic (CEM) models, it has now become possible to extend the CATR electromagnetic simulation to encompass the complete CATR AUT pattern measurement process thereby permitting quantifiable accuracies to be easily determined prior to actual measurement [2, 3, 4, 5]. As the accuracy of these models is paramount to both the design of the CATR and the subsequent determination of the uncertainty budget, this paper presents an accuracy evaluation of five different CEM simulations. We report results using methods of CATR modelling including: geometrical-optics with geometrical theory of diffraction [6], plane-wave spectrum [7], Kirchhoff-Huygens [7] and current elements [8], before presenting results of their use in the antenna pattern measurement prediction for given CATR-AUT combinations that allow 360° far-field patterns to be obtained.

II. Overview of the CATR Configuration

A schematic representation of the geometry of a CATR configuration can be seen presented in Figure 1. Here, the parabolic reflector had a 3.6576 m (12 foot) focal length. The surface profile of the CATR was assumed to be formed from a concave paraboloidal surface. The reflector surface must be a paraboloid of revolution so that the, assumed spherical, incident wave propagating from the focus of the reflector is collimated into a pseudo plane-wave, represented by the green cylinder shown in Figure 1.

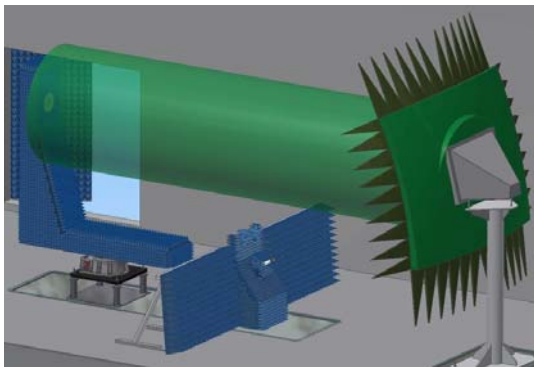

Figure 1. Schematic representation of serrated edge single offset-reflector 2m x 2m QZ CATR being modelled.

The CATR reflector edge treatment comprised serrations that were formed from triangular petals. The phase center of the feed was placed at the focus of the offset reflector and the feed was tilted in elevation by 28°. An 11 dBi WR430 circular choked waveguide was used for the feed with far-field pattern

data being provided by a proprietary full-wave three-dimensional CEM solver using the finite difference time-domain technique. The origin of the CATR co-ordinate system was located at the vertex of the parabolic reflector with the QZ simulations being computed across a transverse plane at z = 1.*8f* where f was the focal length.

III. Overview of Simulation Methods

The following sections provide an overview of the modelling CEM methods harnessed before showing how these can be used to provide simulations of far-field antenna pattern measurement predictions for given CATR-AUT combinations.

A. Introduction to Modelling Methods

The field illuminating the CATR reflector can be determined from far-field antenna pattern function of the feed by reintroducing the spherical phase function and spherical loss factor. The fields reflected by the, assumed perfect electrical conductor (PEC) surface can be obtained from the physical optics condition [8]. Many different CEM modelling techniques have been harnessed for the prediction of fields in the Fresnel-region and these are described in detail within the following sections.

1) Vector Huygens Method (PWS Method)

The vector Huygens principle can be obtained directly from the co-ordinate free form of the plane-wave spectrum method (PWS) and can be expressed as [7],

$$d\underline{E}_p(P) = \frac{jda}{\lambda}\hat{\underline{u}}_r \times (\underline{E} \times \hat{\underline{n}})\psi \qquad (1)$$

Here, ψ is the free space Green's function, $\underline{E}$ is the reflected electric field, $\underline{n}$ is the unit surface normal and $\underline{u}_r$ is the direction to the field point P located at (x, y, z), which must be in the far-field of the infinitesimal radiating elemental Huygens source, resulting in the field point being removed from the Huygens source by a few wavelengths. Thus, the total field at a point in space can be expressed by integrating across the complete, unshaded, reflector surface.

2) Kirchoff Huygens Method

The Kirchhoff-Huygens method is a general technique for determining the field in a source and sink free region outside a surface from knowledge of the field distribution over that closed surface [7]. It is applicable to arbitrary but not necessarily smoothly shaped apertures over which the tangential components of the electric *and* magnetic fields are prescribed. The Kirchhoff-Huygens method is in essence a direct integral of Maxwell's equations. The general vector Kirchhoff-Huygens formula can be expressed as [7],

$$d\underline{E}_p = \frac{da}{4\pi}\left[-j\omega\mu(\hat{\underline{n}} \times \underline{H})\psi + (\hat{\underline{n}} \times \underline{E}) \times \nabla\psi + (\hat{\underline{n}} \cdot \underline{E})\nabla\psi\right] \qquad (2)$$

In addition to the reflected electric fields $\underline{E}$, this expression requires knowledge of the tangential components of the reflected magnetic fields $\underline{H}$. These can be computed from the incident magnetic fields using the method of images [8],

3) Current Elements Method

The current elements method is an alternative field propagation method to those developed above. The current element method replaces the fields with an equivalent surface current density $\underline{J}_s$ which is used as an equivalent source to the original fields. The surface current density across the surface of the reflector can be obtained from the incident magnetic fields and the surface unit normal and is known as the physical-optics approximation [8]. The fields radiated by an infinitesimal electric current element can be obtained from the vector potential & the free-space Green's function using [6, 8],

$$d\underline{H}(P) = \frac{da}{4\pi}\underline{J}_s \times \nabla\psi \qquad (3)$$

The corresponding elemental electric fields can be obtained, to a very good approximation, from the elemental magnetic fields using the far-field TEM condition where again, the field point only need be in the far-field of the elemental source which is a requirement that is easily satisfied when the separation is larger than a few wavelengths.

4) Other Simulations – GO+GTD & FEKO PO

Two further simulations were utilized within the validation campaign. These were obtained from proprietary modelling software that used geometrical optics with geometrical theory of diffraction edge correction, courtesy of The Ohio State University [9], and FEKO physical optics (and large physical optics) solvers [10]. The following section describes how these field propagation models can be used to produce complete far-field antenna pattern measurement predictions for given CATR-AUT combinations.

B. Introduction to Reaction Theorem

The reaction theorem is a well-known method for analyzing coupling problems [2, 7]. This theorem states that, provided the electric and magnetic field vectors ($\underline{E}_1$, $\underline{H}_1$) and ($\underline{E}_2$, $\underline{H}_2$) are of the same frequency and monochromatic then the mutual impedance, Z_{21}, between two radiators, antenna 1 and 2, in the environment described by ε, μ can be expressed in terms of a surface integration [7],

$$Z_{21} = \frac{V_{21}}{I_{11}} = -\frac{1}{I_{11}I_{22}}\int_{S_2}(\underline{E}_2 \times \underline{H}_1 - \underline{E}_1 \times \underline{H}_2) \cdot \hat{\underline{n}}\, ds \qquad (4)$$

Here, $\underline{n}$ is taken to denote the outward pointing surface unit normal. The subscript 1 denotes parameters associated with antenna 1 whilst the subscript 2 denotes quantities associated with antenna 2, *i.e.* S_2 is a surface that encloses antenna 2, but not antenna 1. Here, I_{11} is the terminal current of antenna 1 when it transmits and similarly, I_{22} is the terminal current of antenna 2 when it transmits. Note that this integral does *not* compute transferred power as there are no conjugates present and as such, crucially, phase information is preserved. From reciprocity, the mutual impedance, $Z_{12} = Z_{21}$, and is related to the coupling between two antennas. Clearly then the mutual impedance will also be a function of the displacement between the antennas, their relative orientations, and their respective polarization properties. As an admittance is merely the reciprocal of an impedance, an admittance matrix [Y]

representing this two port coupled systems can be readily populated so that,

$$[Y]=\begin{bmatrix} Y_{11} & Y_{12} \\ Y_{21} & Y_{22} \end{bmatrix} \tag{5}$$

It is well known that the re-normalized scattering matrix, $[S_\Omega]$, can be calculated from this admittance matrix and is used to describe what fraction of the signal is transmitted, or reflected at each port of the coupled system [7],

$$[S_\Omega]=\sqrt{[Y_\Omega]}([Z]-[Z_\Omega])([Z]+[Z_\Omega])^{-1}\sqrt{[Z_\Omega]} \tag{6}$$

Here, $[Y_\Omega] = [Z_\Omega]^{-1}$ and is a diagonal matrix with the desired normalizing admittance as the diagonal entries, *i.e.* the admittance of the attached transmission line which in this case will be equal to the port impedance $Z_1 = Z_2 = Z_{TE}$. The elements $S_{1,2} = S_{2,1}$ of $[S_\Omega]$ are the complex transmission coefficients for the coupled antenna system which are taken to represent a single point in the far-field measurement. When utilizing this procedure to simulate CATR measurements it is crucial to recognize that the fields illuminating the AUT from the CATR only need to be computed once per frequency. This is also true for the fields radiated by the AUT. Thus, in principle, it is possible to simulate measured cuts and patterns in a computationally efficient manner allowing simulation of many different test configurations. This will be further examined in the following section.

IV. Simulation Results

The five different CEM modelling techniques described above were used to compute QZ performance predictions for the offset reflector CATR of Figure 1 at a frequency of 2.6 GHz. The five simulations all used the same feed pattern and range geometry with only the field propagation methodology and reflection calculation changing between the respective simulations. The simulations were: Geometrical Optics with Geometrical Theory of Diffraction edge correction (GO+GTD), Vector Huygens (VH), Kirchhoff Huygens (KH), Current Elements (CE) and FEKO Physical Optics (FEKO). Figure 2 below presents a comparison of the CATR QZ amplitude predictions for the five simulations for the horizontally polarized electric field component (E_x) in terms of iso-levels (contours) where each of the patterns was normalized to 0 dB at the peak of the pattern.

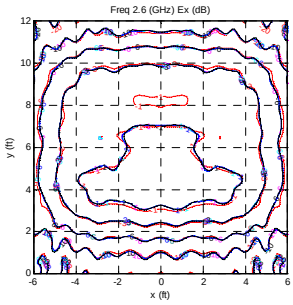

Figure 2. Comparison of E_x polarized QZ amplitude patterns.

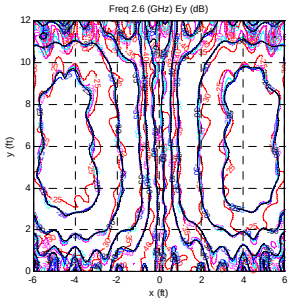

Figure 3. Comparison of E_y polarized QZ amplitude patterns.

Here, red contours denote GO+UTD, magenta contours denote VH, cyan contours denote KH, blue contours denote CE based field propagation, whilst black contours represent the results from FEKO using PO. Figure 3 contains an equivalent plot for the vertically polarized (cross-polar) electric field component, (E_y). From inspection of these plots it is clear that the VH, KH and CE based methods are in very good agreement with GO+GTD being in only very slightly less close agreement, with the main difference being the presence of additional ripple on the GO+GTD QZ predictions. The general levels and shape of all of the patterns, for both the *x*- and *y*-polarized field amplitude plots are very encouraging. Some asymmetry is apparent in the GO+GTD simulations on the *y*-polarized (cross-polarized) patterns, which is erroneous as the model is inherently symmetrical in the *yz*-plane. The feed model is not quite perfectly symmetrical which was an artefact of small numerical imperfections within the CEM model that was used to generate the feed pattern predictions. A more detailed, quantitative, analysis of the degree of agreement between these respective results can be found in the open literature [11] together with additional comparison plots, where further confirmation of the excellent agreement between the FEKO PO and CE methods was demonstrated.

The simulations presented above are based upon propagating those fields from the feed that are incident on the CATR reflector and arrive at the QZ. However, as a consequence of the geometry of the offset reflector CATR, it is possible for the back-lobe of the feed antenna to directly illuminate the QZ. In practice a great deal of time, trouble, and effort is invested in minimizing this, which involves the use of absorber collars or/and absorber baffles, [1]. However, as part of the CATR design process it is useful to be able to determine the upper bound, *i.e.* worst case performance, when feed spill-over impinges on the QZ unimpeded. Figures 4 & 5 present E_x and E_y amplitude plots that compare the FEKO PO (red-contours) and the CE QZ predictions for the ideal case where there is no direct illumination of the QZ, *cf.* Figures 2 and 3.

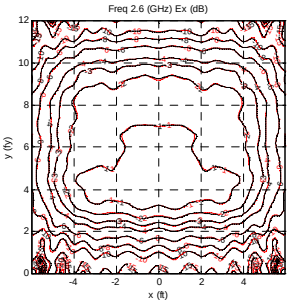

Figure 4. Comparison of E_x polarized QZ amplitude patterns.

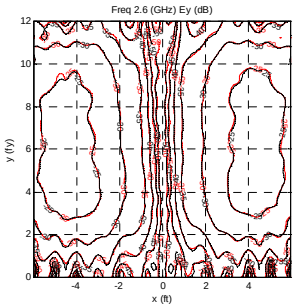

Figure 5. Comparison of E_y polarized QZ amplitude patterns.

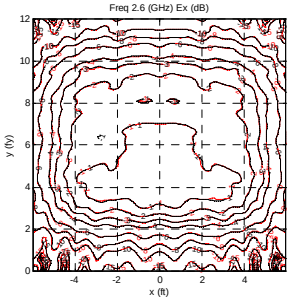

Figure 6. Comparison of E_x polarized QZ amplitude patterns.

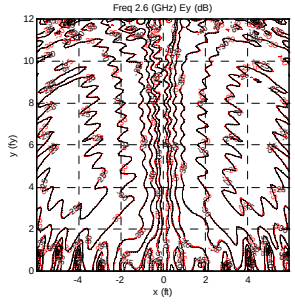

Figure 7. Comparison of E_y polarized QZ amplitude patterns.

Conversely, Figures 6 and 7 present equivalent results for the case where the back lobe of the feed is permitted to directly illuminate the QZ, based on a feed that has approximately -23 dBi gain in the direction of the QZ center. As before the agreement between the FEKO PO and CE simulations are excellent with contours overlaying down to the -60 dB levels thereby lending a great deal of confidence that the models are implemented correctly. As expected, for the case where the direct and reflected fields interfere through linear superposition, additional ripple is introduced onto the pseudo plane-wave through constructive and destructive interference. This is in agreement with what is observed in actuality and is the principal reason for the use of absorber treatments so as to minimize feed spillover [1].

The CATR is inherently a very broad-band antenna test solution being limited, primarily, at low frequency by the electrical size of the reflector(s) and at high frequencies by manufacturing tolerance, *e.g.* reflector surface accuracies & roughness [1]. Thus, to illustrate the ability of the CEM simulations to obtain a similar degree of agreement across a broader range of frequencies comparisons were also made at 10, 30, and 40 GHz with, as a result of the need for brevity, comparisons being presented below for the more demanding 40 GHz case. Figures 8 to 11 contain horizontal and vertical amplitude and phase plots through the center of the QZ that are intended to allow a critical assessment of the degree of agreement to be attained. Here, red traces denote QZ data as obtained from FEKO large PO solver, whilst the black traces denote results obtained from the CE field propagation. In each of these simulations, QZ feed spill-over has been omitted. In practice, for a CATR to be able to measure the main and cross-polarized field components of an AUT the CATR feed would need to be rotated by 90° about its axis thus the following simulations also show predicted CATR QZ plots for the case where the feed was sequentially *x*- and *y*-polarized within its local co-ordinate system.

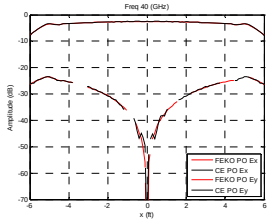

Figure 8. Comparison H-cut, E_y polarized QZ amplitude, V-pol feed.

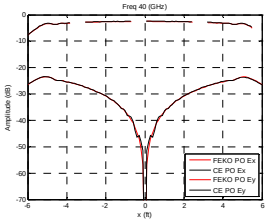

Figure 9. Comparison H-cut, E_x polarized QZ amplitude, H-pol feed.

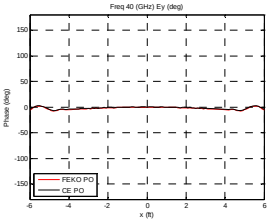

Figure 10. Comparison H-cut, E_y polarized QZ phase, V-pol feed.

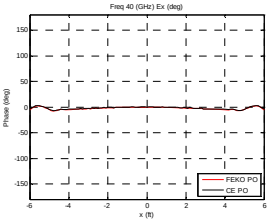

Figure 11. Comparison of H-cut, E_x polarized QZ phase, H-pol feed.

Here, it is clear that all of the principal polarized cardinal cuts are in excellent agreement with the general pattern shapes and features being in very close agreement. The CE predictions exhibits some low amplitude high spatial frequency ripple that is missing from the FEKO PO model. The absence of the fine structure in the FEKO PO predictions is expected and is a consequence of the use of large element approximation within the solver, which was a necessary introduction that resulted from extended simulation times. General cross-polar levels were also found to be in excellent agreement, with only the null-depth changing between the simulations. The phase patterns are also in very good agreement again confirming adoption of the same time dependency. Although not shown, some small phase differences are evident but only in regions of low field intensity where it is difficult to control phase, *e.g.* in nulls and towards the extremities of the QZ.

As stated above, the coupling of the pseudo plane-wave into the aperture of an AUT creates the classical measured "far-field" radiation pattern and can be evaluated by performing the integration expressed within equation (4). This integration can be performed across any convenient free-space closed surface. Although some workers have successfully evaluated this integral across planar surfaces [2] a more powerful, generic, CATR modelling procedure can be developed if instead a spherical surface is utilized. Figures 12 and 13 illustrate respectively the *x*- and *y*-polarized electric near-fields of an AUT sampled across the surface of sphere of radius of 0.6096 m (24"). Here, the amplitude patterns are presented in terms of false-color plots over the conceptual spherical integrating surface. Although not shown, the *z*-polarized electric field and corresponding magnetic fields were also obtained from a simple CEM model [1]. The corresponding far-fields were also determined and are shown below where they are used as a "truth" model against which the CATR measurement simulation can be gauged. Figure 14 and 15 present equivalent plots for the case where the AUT has been rotated by 40° about the positive *y*-axis as would be required when evaluating the corresponding "measured" far-field pattern value at this angle.

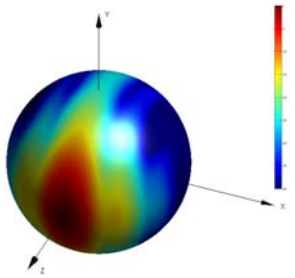

Figure 12. E_x polarized AUT near-field amplitude pattern.

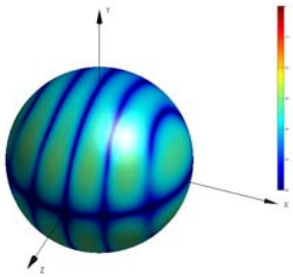

Figure 13. E_y polarized AUT near-field amplitude pattern.

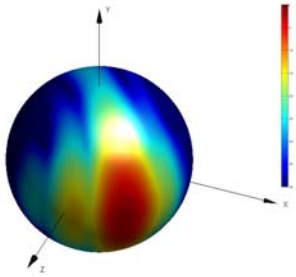

Figure 14. E_x polarized rotated AUT near-field amplitude pattern.

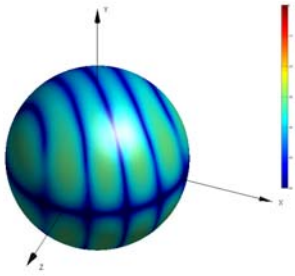

Figure 15. E_y polarized rotated AUT near-field amplitude pattern.

Although any closed surface could be used, the advantage of the spherical integration surface is that a general compound rotation about the *x*-, *y*- and *z*-axes can be implemented without the need to compute fields outside this sampling interval, *i.e.* domain. Such vector isometric rotations can be implemented either approximately through approximation [1, 7] or rigorously by expanding the fields onto a set of spherical vector mode functions and by rotating those functions [1]. In most cases, the choice is unimportant as the near-fields can be grossly over sampled, to improve the accuracy of the numerical integration, so that the use of approximation typically introduces only second order errors. However, if the fields are sampled on an azimuth over elevation tabulating co-ordinate system the pattern rotation is reduced to a cyclic permutation of the column elements within the data array thereby eliminating this source of error. Thus, in this case, the number of points in the azimuth axis of the near-field data was set equal to the number of points in the required far-field great-circle azimuth simulated measurement cut. Adoption of an elevation over azimuth co-ordinate system would enable the elevation cut to be obtained in a similarly rigorous fashion.

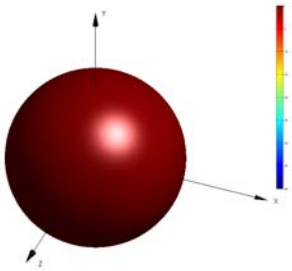

Figure 16. Comparison of E_x polarized QZ amplitude patterns.

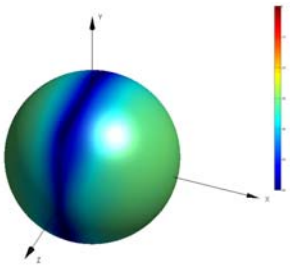

Figure 17. Comparison of E_y polarized QZ amplitude patterns.

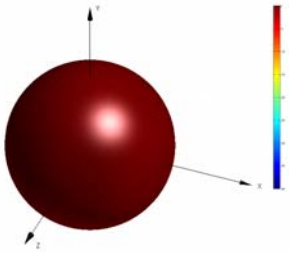

Figure 18. Comparison of E_x polarized QZ amplitude patterns.

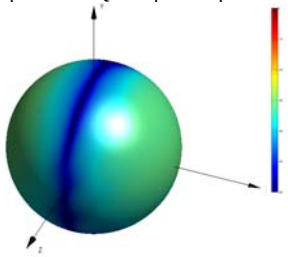

Figure 19. Comparison of E_y polarized QZ amplitude patterns.

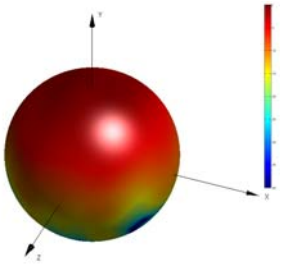

Figure 20. Comparison of E_x polarized QZ amplitude patterns.

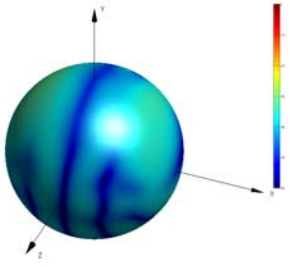

Figure 21. Comparison of E_y polarized QZ amplitude patterns.

Figure 16 and 17 present, respectively, the E_x and E_y polarized fields of the pseudo plane wave as created by the CATR. Although the CATR QZ data presented above were sampled across the surface of a plane that was transverse to the z-axis of the range, in principle fields can be computed at any point in space providing that point is more than a few wavelengths from the surface of the reflector and outside of the geometric shadow region. Consequently, it is possible to place the spherical integrating surface in various positions throughout the QZ. This corresponds to making a measurement with the AUT located at different positions within the QZ. Figures 18 and 19 present corresponding CATR QZ data for the case where the sphere was translated to the bottom of the QZ where the zenith of the sphere was aligned with the bottom of the CATR reflector (before the serrations started). Conversely, Figure 20 and 21 show equivalent patterns for the case where the origin of the sphere was aligned with a projection of the vertex of the parabolic reflector, *i.e.* the sphere located half outside of the CATR QZ in what is far from an optimum position. Here, it is possible to clearly see the degradation in the performance of the pseudo plane wave at the extremities as the uniformity in the amplitude of the *x*-polarized electric field is greatly reduced, *cf.* Figure 20 and Figure 16. Thus, by computing the reaction of the sequentially rotated AUT (as illustrated in Figures 12 – 15) with the translated CATR fields (as illustrated in Figures 16 – 21) it is possible to compute, in a very general sense, the simulated far-field CATR measurement of a given AUT.

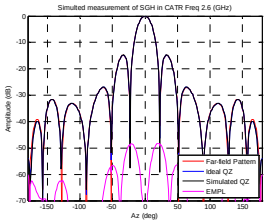

Figure 22. Comparison of E_x polarized QZ amplitude patterns.

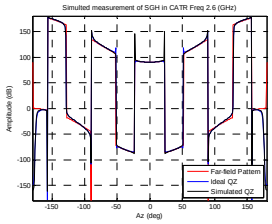

Figure 23. Comparison of E_y polarized QZ amplitude patterns.

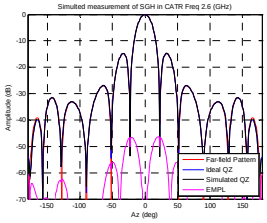

Figure 24. Comparison of E_x polarized QZ amplitude patterns.

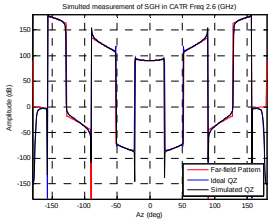

Figure 25. Comparison of E_y polarized QZ amplitude patterns.

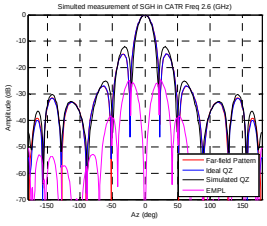

Figure 26. Comparison of E_x polarized QZ amplitude patterns.

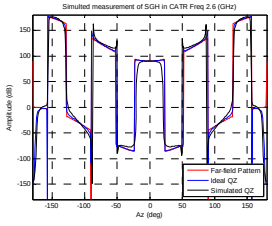

Figure 27. Comparison of E_y polarized QZ amplitude patterns.

The red trace that can be seen in Figure 22 contains a plot of the ideal far-field pattern of the 2.6 GHz AUT (that was used to compute the spherical near-fields shown in Figures 12 and 13). The blue trace corresponds to specifying the pseudo plane wave as being that of a perfect TEM wave propagating in the z-axis and then using the reaction integral to evaluate the coupled fields. This process of rotating and integrating implements a spherical near-field to far-field transform. The agreement between the red and blue traces for the amplitude and phase

plots (Figure 23) confirms the validity of the approach. The black trace denotes the simulated measured far-field pattern that is obtained when using the pseudo plane wave that is generated by the offset parabolic reflector CATR. Here, from inspection of the agreement between the simulated measured far-field pattern and the ideal far-field amplitude and phase patterns is very encouraging. This is further corroborated by the low level of the equivalent multipath level (EMPL) trace [1, 7], shown in magenta on Figure 22. The EMPL is a quantitative objective measure of the adjacency between two patterns with better agreement being denoted with increasing large negative dB values. Here, the peak EMPL between the ideal and simulated measured far-field pattern is *circa* -48 dB. When the AUT is translated to the lower edge of the CATR QZ it can be seen that the degree of agreement slightly degrades as the EMPL level, as shown in Figure 24, increases by circa 2 dB. However, once the AUT is translated so as to be situated level with the vertex of the reflector, *i.e.* outside of the classical QZ region, it is clear that from inspection of Figure 26 the simulated CATR measurement is grossly distorted with significant differences becoming apparent and the peak EMPL level increasing to circa -16 dB. This is to be expected and is further confirmation that this new CATR measurement simulation is producing reliable results. Crucially, the CATR simulation technique is also able to provide phase data *cf.* Figure 23. This is a crucial feature of the very general simulation technique.

By way of a further confirmation, and verification that this technique could be utilized at higher frequencies involving electromagnetically larger problems, this simulation was repeated for the case of an x-band (10 GHz) antenna. Similarly, results for the case where the AUT was located at the center of the QZ and for the case where the AUT was situated at the lower edge of the QZ can be found presented in Figures 28 and 29, and Figures 30 and 31 respectively. As before, the EMPL was computed and can be seen presented in the figures as the magenta trace. As was previously noted the peak EMPL increases slightly, *circa* 6 dB, as the AUT is positioned towards the extremities of the QZ.

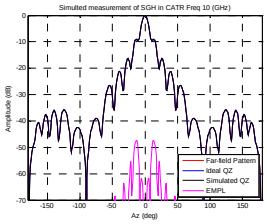

Figure 28. Comparison of E_x polarized QZ amplitude patterns.

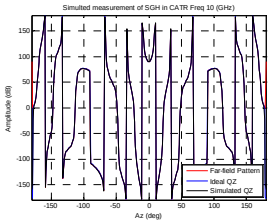

Figure 29. Comparison of E_y polarized QZ amplitude patterns.

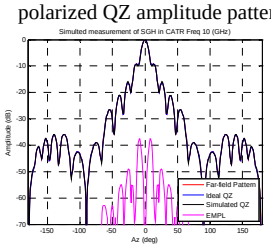

Figure 30. Comparison of E_x polarized QZ amplitude patterns.

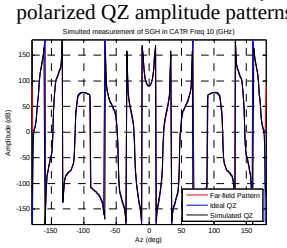

Figure 31. Comparison of E_y polarized QZ amplitude patterns.

Here, in both the *s*- and *x*-band simulations it can be seen from the EMPL result that the largest uncertainties are located in the near pattern angle with perhaps the peak of the first side-lobe level suffering from the largest error, *cf.* [4, 12]. This is in agreement with what is commonly observed in practice when using a "far-field" direct antenna pattern measurement when the incident plane wave has quadratic phase error resulting from different far-field distances [8].

V. Summary And Conclusions

This paper presented the preliminary results of an extensive validation campaign for a new CATR CEM simulation tool that permits the derivation of the error to signal level for a specified AUT and CATR combination. Thus, for the first time, in addition to being able to provide conventional CATR QZ performance predictors such as amplitude taper, amplitude and phase peak-to-peak ripple, it is also possible to provide full-sphere simulated measured data for a given CATR AUT combination. The future work is to include obtaining further numerical verification of the FF-MARS multipath suppression technique.

Acknowledgement

The Ohio State University for providing GO+GTD CATR QZ simulation data.

References

[1] C.G. Parini, S.F. Gregson, J. McCormick, D. Janse van Rensburg "Theory and Practice of Modern Antenna Range Measurements", IET Press, 2014, ISBN 978-1-84919-560-7.

[2] M. Philippakis, C.G. Parini, "Compact Antenna Range Performance Evaluation Using Simulated Pattern Measurements", IEE Proc. Microw. Antennas Propag., Vol. 143, No. 3, June 1996, pp. 200-206.

[3] D. Fasold, "Measurement Performance of Basic Compact Range Concepts", AMTA Europe Symposium, Munich, 2006.

[4] C. Cappellin, S. Busk Sørensen, M. Paquay, A. Østergaard, "An Accurate and Efficient Error Predictor Tool for CATR Measurements", EuCAP 2010), Barcelona, April 2010.

[5] A. Muñoz-Acevedo, M. Sierra-Castañer, J. L. Besada, "Efficient and Accurate hybrid GO-Spectral Algorithm to Design Conformal Serrated-Edge Reflectors Operating as Collimators in Millimeter Wave Compact Ranges", INVE MEM 2010.

[6] G.L. James, "Geometrical Theory of Diffraction for Electromagnetic Waves", 3rd Edition, IET Press, 2007.

[7] S.F. Gregson, J. McCormick, C.G. Parini, "Principles of Planar Near-Field Antenna Measurements", IET Press, 2007.

[8] A.W. Rudge, K.Milne, A.D. Olver, P. Knight, "The Handbook of Antenna Design Volume I", IEE Press, 1982.

[9] T.-H. Lee, "Geometrical Optics And GTD Analysis of Subreflectors in Cassegrain and Gregorian Reflector Antennas", MSc Thesis, The Ohio State University, 1984.

[10] EM Software & Systems, FEKO Suit 7.0, www.feko.info.

[11] C.G. Parini, R. Dubrovka, S.F. Gregson, "Compact Range Quiet Zone Modelling: Quantitative Assessment using a Variety of Electromagnetic Simulation Methods", Loughborough Conference on Antennas and Propagation, Loughborough, November, 2015.

[12] F. Jensen, K. Pontoppidan, "Modelling of the Antenna-to-Range Coupling For a Compact Range", AMTA, Denver Colorado, October, 2001.